



Cite this: *Energy Environ. Sci.*,
2019, 12, 640

Efficient CO₂ to CO electrolysis on solid Ni–N–C catalysts at industrial current densities†

Tim Möller,^{‡,a} Wen Ju,^{‡,a} Alexander Bagger,^{‡,b} Xingli Wang,^a Fang Luo,^a Trung Ngo Thanh,^a Ana Sofia Varela,^c Jan Rossmeisl^b and Peter Strasser^{‡,a*}

The electrochemical CO₂ reduction reaction (CO₂RR) to pure CO streams in electrolyzer devices is poised to be the most likely process for near-term commercialization and deployment in the polymer industry. The reduction of CO₂ to CO is electrocatalyzed under alkaline conditions on precious group metal (PGM) catalysts, such as silver and gold, limiting widespread application due to high cost. Here, we report on an interesting alternative, a PGM-free nickel and nitrogen-doped porous carbon catalyst (Ni–N–C), the catalytic performance of which rivals or exceeds those of the state-of-the-art electrocatalysts under industrial electrolysis conditions. We started from small scale CO₂-saturated liquid electrolyte H-cell screening tests and moved to larger-scale CO₂ electrolyzer cells, where the catalysts were deployed as Gas Diffusion Electrodes (GDEs) to create a reactive three-phase interface. We compared the faradaic CO yields and CO partial current densities of Ni–N–C catalysts to those of a Ag-based benchmark, and its Fe-functionalized Fe–N–C analogue under ambient pressures, temperatures and neutral pH bicarbonate flows. Prolonged electrolyzer tests were conducted at industrial current densities of up to 700 mA cm⁻². Ni–N–C electrodes are demonstrated to provide CO partial current densities above 200 mA cm⁻² and stable faradaic CO efficiencies around 85% for up to 20 hours (at 200 mA cm⁻²), unlike their Ag benchmarks. Density functional theory-based calculations of catalytic reaction pathways help offer a molecular mechanistic basis of the observed selectivity trends on Ag and M–N–C catalysts. Computations lend much support to our experimental hypothesis as to the critical role of N-coordinated metal ion, Ni–N_x, motifs as the catalytic active sites for CO formation. Apart from being cost effective, the Ni–N–C powder catalysts allow flexible operation under acidic, neutral, and alkaline conditions. This study demonstrates the potential of Ni–N–C and possibly other members of the M–N–C materials family to replace PGM catalysts in CO₂-to-CO electrolyzers.

Received 11th September 2018,
Accepted 13th December 2018

DOI: 10.1039/c8ee02662a

rsc.li/ees

Broader context

Advances towards a circular economy, in which CO₂ is used as feedstock for large-scale fabrication of carbon-based fuels and manifold chemicals, is of utmost scientific and technological interest to meet the challenges of a sustainable society. The electrochemical CO₂ reduction reaction to CO streams with controlled selectivity has the potential to contribute to this circular economy as it can be coupled to well-established industrial processes, such as the methanol carbonylation, phosgene-based processes or the Fischer–Tropsch reaction, to effectively integrate renewable electricity into the production of value-added chemicals and fuels. To realize this carbon neutral circle, the development of effective catalysts is crucial for efficient and selective electrolysis to achieve sufficient CO-yield for industrial applications. In this study, we present a nickel and nitrogen-doped porous carbon-catalyst, which rivals the catalytic CO₂-to-CO activity and selectivity of the state-of-the-art precious metal group catalysts, such as silver and gold. We use gas diffusion electrodes to create a reactive three-phase interface, to perform electrolysis at current densities of industrial relevance in a flow electrolyzer. Selective and high yield production of CO on our catalyst is demonstrated. Density functional theory-based calculations support our observation and demonstrate beneficial binding energies for CO evolution on this cost-effective catalyst.

^a The Electrochemical Energy, Catalysis, and Materials Science Laboratory, Department of Chemistry, Chemical Engineering Division, Technical University Berlin, Berlin, Germany. E-mail: pstrasser@tu-berlin.de

^b Department of Chemistry, University Copenhagen, Universitetsparken 5, 2100 Copenhagen, Denmark

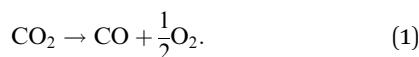
^c Institute of Chemistry, National Autonomous University of Mexico, Mexico City, Mexico

† Electronic supplementary information (ESI) available. See DOI: 10.1039/c8ee02662a

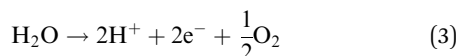
‡ These authors contributed equally to this work.

Growing CO₂ emissions with their detrimental environmental effects have prompted the search for innovative scalable technologies for CO₂ reuse.^{1,2} Among the emerging technologies to convert CO₂ to valuable carbon-based fuels or chemicals, the direct electrochemical CO₂ reduction reaction on solid catalysts at ambient pressures and temperatures in pH neutral environments, henceforth referred to as the “CO₂RR”, has emerged as a particularly promising candidate due to its immediate link to renewable input electricity to drive the overall process.^{3,4} Overall faradaic efficiencies and chemical selectivities of the CO₂RR are strongly dependent on the chemical and structural nature of the employed electrocatalysts in the electrodes of the CO₂ electrolyzer device.⁵ Metallic or partially oxidized copper is the catalyst of choice for its unique property of reducing CO₂ via CO into ethylene and ethanol.⁶ Plenty of studies have therefore been conducted to understand and improve its catalytic performance.^{7–18} Unfortunately, the excessive kinetic overpotentials required to drive the CO₂ reduction to ethylene and ethanol combined with the limited faradaic efficiencies keep the overall energy efficiency of this process prohibitively low.^{8,19}

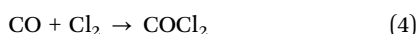
A commercially much more interesting electrocatalytic reaction cascade represents the direct 2-electron CO₂-to-CO pathway according to



This overall reaction splits into the half-cell reactions



at the cathode and anode of a CO₂ electrolyzer. This process was studied on precious metal catalysts, such as Au or Ag, which have demonstrated the largest CO efficiencies to date.^{6,20–25} Pure CO streams are industrially used as intermediates in the production of polycarbonate and polyurethane polymers, where CO is reacted with chlorine to yield phosgene according to⁵⁰



which is immediately turned into isocyanates and polycarbonates. While CO remains in the monomer, chlorine is recovered as HCl. It is not unfeasible that, one day, electrode reaction (2) will be coupled with the electrocatalytic chlorine evolution reaction into a direct CO₂/brine-to-CO/Cl₂ electrolyzer, which would supply both key intermediates in a combined 200% electrocatalytic process, according to



The cathodic CO₂-to-CO catalysis cascade requires cathode electrocatalyst materials that can sustain industrial current densities of up to several hundred (mA cm⁻²) geometric electrode area over extended periods of time under ambient conditions and benign pH conditions, while remaining highly selective for CO. Although Ag and Au are perceived as state-of-the-art electrocatalysts for the CO₂-to-CO process, their limited faradaic efficiencies at large current densities, and the required high

alkaline pH of 14 and higher in order to unfold their activity combined with their prohibitively large materials cost hamper any wider commercial application. Studies employing Ag catalysts are typically performed in aggressive alkaline catholytes, while the use of Ag under neutral pH conditions resulted invariably in lower activity.^{18,26,27}

This is why the search for new precious group metal (PGM)-free, yet efficient and durable electrocatalysts deployable in scaled-up cathode layer electrode designs supporting CO₂ reduction at industrial current densities is currently an important scientific and technological priority.

Recent computational and experimental works have expanded our horizon with regard to active and CO-efficient CO₂RR catalysts. Transition metal (M)- and nitrogen-doped high surface area carbon materials (henceforth referred to as “M-N-C”) were put forward as promising solid, yet non-metallic candidates for the catalytic CO₂ to CO reduction process. A chemical porphyrin-like M-N_x motif, where a central metal ion is coordinatively bonded in-plane to up to four pyridinic N atoms, embedded in the surface of the solid carbon catalysts was shown to act as the active site of the CO₂ reaction process.²⁸ In comparison to Ag or Au catalysts, the isolated active single M-N_x sites hold the important advantage of largely suppressing the competing Hydrogen Evolution Reaction (HER) process, due to unfavorable chemisorption of atomic hydrogen on and near the M-N_x sites. This enhances the chemical selectivity and faradaic efficiency towards CO₂ reduction significantly.²⁹ The chemical flexibility in the choice of the metal M of the M-N-C materials offers a diverse set of M-N-C catalyst candidates for CO₂RR utilization.^{30–34} In 2015, Varela performed the CO₂ reduction on Fe-N-C catalysts and observed up to 80% CO selectivity at electrode potentials of -0.6 V_{RHE}.^{35–37} Follow up catalyst screening evidenced that the Fe-N_x motif,³⁶ however, exhibited good CO faradaic efficiencies only at moderately cathodic electrode potentials of around -0.6 V_{RHE}, while at larger overpotentials the HER process outperformed and resulted in a sharp drop in CO selectivity. Chemically reactive Ni-N_x motifs, in contrast, *i.e.* the active moiety of solid Ni-N-C electrocatalysts, produced CO with good selectivities at larger current densities and kinetic overpotentials.^{36,38–42} Jiang *et al.* reported a Ni-N-graphene catalyst, which provided roughly 50 mA cm⁻² CO partial current density (j_{CO}) with an MEA at 2.78 V cell voltage.⁴¹ In another study, CO production activity reached 70 mA cm⁻² at -1.03 V_{RHE} in a regular H-cell on porous carbon substrates.⁴⁰ However, to achieve technological viability, much higher current densities and CO yields must be demonstrated without any loss in efficiency.

In this contribution, we demonstrate the first successful deployment of PGM-free solid Ni-N-C electrocatalysts for the electrocatalytic CO₂-to-CO reduction in a gas diffusion electrode (GDE) as part of a Micro Flow Cell (MFC) electrolyzer. At ambient pressures and temperatures and at neutral pH of the anolyte and catholyte we demonstrate unprecedented CO yields at industrial current densities of up to 700 mA cm⁻². Our results evidence the significant activity and efficiency advantages of Ni-N-C catalysts over a commercial Ag/AgO_x catalyst, Fe-N-C as well as metal-free nitrogen-doped catalysts.

We synthesized Fe–N–C and Ni–N–C powder electrocatalysts by mixing and pyrolyzing polyaniline as the N-precursor and a high surface area Ketjen600EC as the carbon source, whereas Fe- and Ni-chloride were used as metal precursors. High-temperature pyrolysis of the precursor mixtures was performed in a N₂ atmosphere at 900 °C for 2 hours, after which residual metal species were leached with H₂SO₄ (details of the catalyst synthesis is provided in the ESI†). This catalyst synthesis is based on a proven recipe for solid PGM-free metal/nitrogen doped carbon powder catalysts previously tested for the oxygen reduction reaction.^{43–45} Fig. 1a schematizes the typical various chemical states of carbon-embedded nitrogen atoms as reported in decade-long past work, including pyridinic, pyrrolic, graphitic, nitrogen oxide, and the metal–N₄ moiety. A metal-free nitrogen-doped carbon powder catalyst (referred to as “N–C”) was synthesized as control. Physico-chemical characterization of the degree of crystallinity and crystalline phases was carried out by using X-Ray Diffraction (XRD). Experimental patterns in Fig. S1 (ESI†) reflect the largely amorphous character of the N–C and Fe–N–C catalysts, whereas residual crystalline inorganic Ni species were detected for the Ni–N–C. The Transmission Electron Microscopy (TEM) images (Fig. 1b–d) and the bulk compositional analysis by ICP-OS (see Table S1, ESI†) agree with our XRD findings, revealing the predominantly amorphous character of the N–C and Fe–N–C catalysts, while carbon-encapsulated particles were visible in the Ni–N–C powder (Fig. S2, ESI†). Specific surface areas of the three catalysts were assessed by N₂ physisorption isotherms (see Fig. S3, ESI†). Table S1 (ESI†) compares the experiment-derived and calculated Brunauer–Emmett–Teller (BET) surface areas: Fe–N–C displayed more than 600 m² g⁻¹, almost 3 times larger than those of the Ni–N–C and metal free

N–C catalysts. A significant rapid N₂ uptake at relative pressures above 0.9 for the Fe–N–C sample (see Fig. S3a, ESI†) suggested rich mesoporosity confirmed by the calculated pore distribution (Fig. S3b, ESI†). All these *ex situ* surface area tests are in line with the *in situ* electrochemical double layer capacity measurements used to independently confirm the trend in the real surface areas among the three carbonous catalysts (see Fig. S4, ESI†). Chemical analysis and nitrogen speciation of the catalyst's surface were conducted using X-ray photoelectron microscopy spectroscopy (XPS) using survey scans (Fig. S5a, ESI†) and high resolution analysis (Fig. S5b–d, ESI†). The surface atomic mole fractions of the metal, nitrogen, oxygen, sulphur, and carbon are given in Table S1 (ESI†). It is noteworthy that even though more than 10 wt% Ni was detected in the bulk, XPS data evidence that the Ni species show a molar fraction of only 0.38% on the catalyst surface, confirming the success of the acid leaching process. This also suggests that the residual encapsulated Ni particles that have resisted the repeated acid leaching procedure must be densely encapsulated in ≥10 nm thick carbon overlayers, as shown by the experimental micrograph in Fig. S2 (ESI†). These Ni particles are therefore probably completely unable to participate in the catalytic CO₂-to-CO reaction process, apart from the fact that Ni particles, due to their electronic surface structure, are unable to reduce CO₂ to CO.⁶ Considering the high resolution photoemission spectra, the N1s core level region (Fig. S5b, ESI† for Ni–N–C) evidenced the presence of the porphyrin-like N-coordinated Ni–N_x moieties at 399.7 eV.^{31,40,46}

Liquid-electrolyte H-cell screening tests

The catalytic performance of the three doped carbon electrocatalysts with respect to the electrochemical CO₂ reduction was first evaluated in a three-electrode, two-compartment liquid-electrolyte H-cell, equipped with an anion exchange membrane between the anode and cathode chamber. The catalyst was immobilized on a mirror-flat glassy carbon plate with a geometric loading of 0.75 mg cm⁻². Additionally, a commercial AgO_x powder catalyst was measured under identical electrochemical conditions as a state-of-the-art metallic benchmark. We note that we continue to refer to this benchmark catalyst as “AgO_x” even though we are aware that the surface of this catalyst reduces to metallic Ag under reaction conditions. The total CO₂RR current densities as a function of iR-corrected working electrode potentials after 15 minutes of stationary constant-potential electrolysis are reported in Fig. 2a. These curves compare and contrast the overall catalytic activity of the four catalysts. Clearly, Fe–N–C and Ni–N–C electrocatalysts exhibited much larger overall current densities over the entire potential range. Online gas chromatography was used to quantify gaseous products and to assess the faradaic product efficiencies. Without exception, CO was the major detectable CO₂RR product, while all residual faradaic charge contributed to the HER process. Due to stronger chemisorption of CO on the Fe–N_x moieties³⁶ compared to Ni–N–C, only the Fe–N–C samples catalyzed the

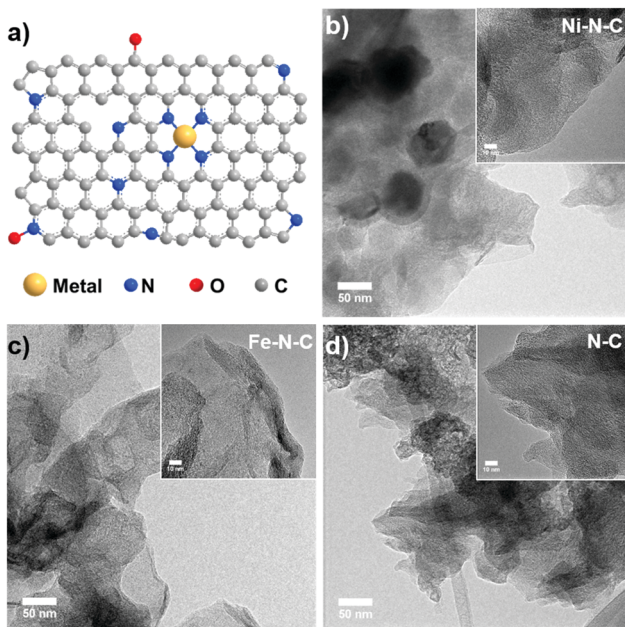


Fig. 1 (a) Illustration of M–N–C catalysts. Representative TEM images of (b) Ni–N–C, (c) Fe–N–C and (d) N–C catalysts. Insets: HR-TEM images of the as-prepared catalysts.

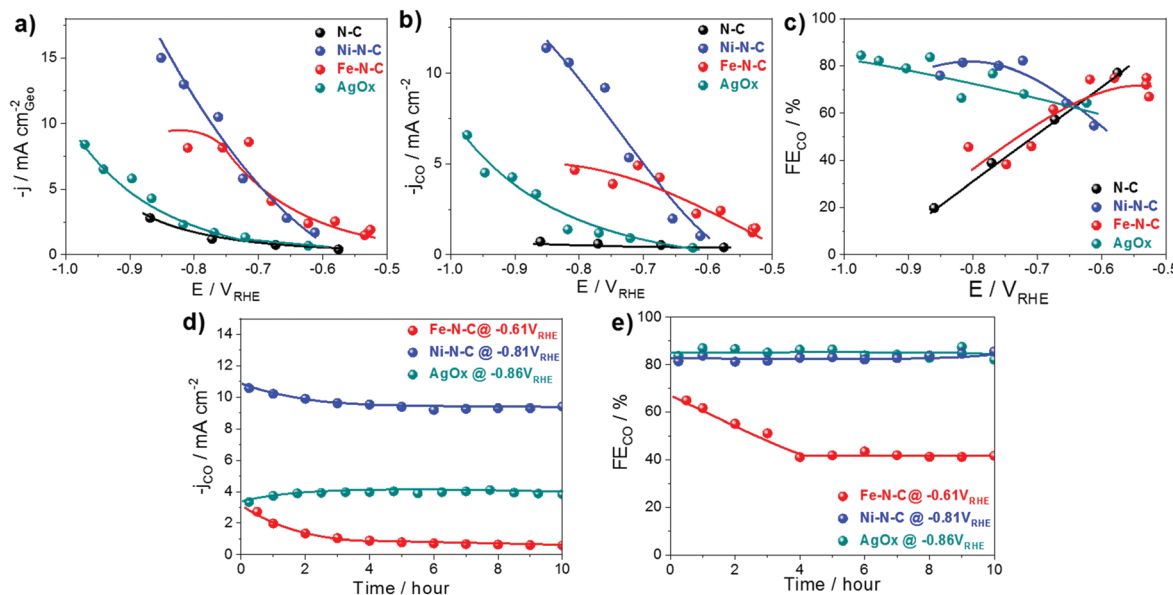


Fig. 2 Catalytic performance and product analysis on N-C (black), Fe-N-C (red), Ni-N-C (blue) and AgO_x (cyan) catalysts. (a) Absolute geometric current densities; (b) geometric CO production current densities; (c) CO faradaic efficiency as a function of applied IR-corrected electrode potential at 15 min of each electrolysis (CO partial current densities and faradaic CH₄ yield are shown in Fig. S6 and S7, ESI†). (d) Geometric CO production current densities and (e) CO faradaic efficiency during the long-term stability testing as a function of stationary electrolysis time. Lines are drawn to guide the eye. Conditions: CO₂-saturated 0.1 M KHCO₃ (pH 6.8) with 0.75 mg cm⁻² catalyst loading.

consecutive protonation of CO to methane, as evidenced in Fig. S7 (ESI†). This makes Fe-N-C an extremely rare example of a non-Cu based CO₂RR catalyst with the capability to reduce CO₂ into “beyond CO” products such as hydrocarbons. No measurable liquid products were found in the electrolyte using High Performance Liquid Chromatography (HPLC) and liquid GC.

Fig. 2b and c display the partial CO current density and the CO efficiency as a function of IR-free potential. The Fe-N-C carbon catalyst showed good CO₂RR reactivity at lower potentials of up to -0.6 V_{RHE} and approached an efficiency maximum.^{36,37,47} In contrast, the metal-free N-C catalyst showed only negligible CO₂RR reactivity, again, indicating that the M-N_x moieties played a dominating mechanistic role in the catalytic reactions.

Despite comparable CO efficiencies of the Ni-N-C and the AgO_x benchmark catalysts at electrode potentials of up to -1.0 V_{RHE}, the CO production on Ni-N-C reached 12 mA cm⁻² at -0.85 V_{RHE}, which was more than twice that of the AgO_x catalyst (7 mA cm⁻² at -0.97 V_{RHE}).

To investigate the durability of the catalysts in the H-cell configuration, 10 hour electrolysis tests were carried out using the Fe-N-C, Ni-N-C and AgO_x catalysts, each at the electrode potentials where their respective maximum CO efficiency was observed. Partial CO current and CO efficiency over time data are plotted in Fig. 2d and e. Both CO partial current and CO efficiency of the Ni-N-C catalyst showed only a minor drop, maintaining more than 90% of its initial performance values. This behavior was comparable to that of the AgO_x catalyst, which, however, displayed a much lower absolute CO yield (see Fig. 2d). In contrast, the Fe-N-C catalyst started to produce more hydrogen until its FE value stabilized after 4 hours. The absolute CO yield was lower than that of the AgO_x catalyst.

We conclude from the screening tests in our H-cell that the performance of the Ni-N-C catalyst equaled or exceeded that of our AgO_x benchmark in terms of CO yield, efficiency and stability.

To understand the experimental activity-selectivity trends, Density Functional Theory (DFT) simulations were carried out for the catalytic reaction process on well-defined Fe-N₄-C and Ni-N₄-C moieties, and were compared to results obtained with a single crystalline Ag(111) surface. The various metal–nitrogen binding schemes of the moieties are illustrated in Fig. 3a. Their corresponding free energies are plotted in Fig. 3b. Finally, a comparison of the free energy diagrams for the CO₂RR and the competing HER pathways on the single-site metal–N₄ motifs and the Ag(111) metal facet is displayed in Fig. 3c and d.

Three considerations can help understand the performance of a catalyst for the CO₂RR to CO under aqueous conditions. First, the initial selectivity can be evaluated by comparing the intermediate binding energy for *COOH (CO₂RR) and *H (HER). Here, Ni-N₄-C and Fe-N₄-C are quite comparable, while Ag(111) shows a relatively stronger *H binding, agreeing with previous theoretical observations.²⁹ Second, the desorption of *CO from the active site has to be fast in order to achieve high rates for CO₂RR, therefore *CO binding has to be weak. Both Ag(111) and Ni-N₄-C do not bind *CO (Fig. 3c), while *CO binds strongly on Fe-N₄-C, indicating problematic kinetics for the Fe catalyst, but potentially enabling further reduction.^{5,36,47} Finally, in order to reduce the required overpotential, binding of *COOH needs to be strong, which is the strongest on the Fe-N-C, intermediate for the Ag(111) and weakest on the Ni-N-C. While we do acknowledge the influence that the detailed coordination (Fig. 3a) or hydrogenated environment (Fig. S8, ESI†) could have on the binding properties of the M-N-C,

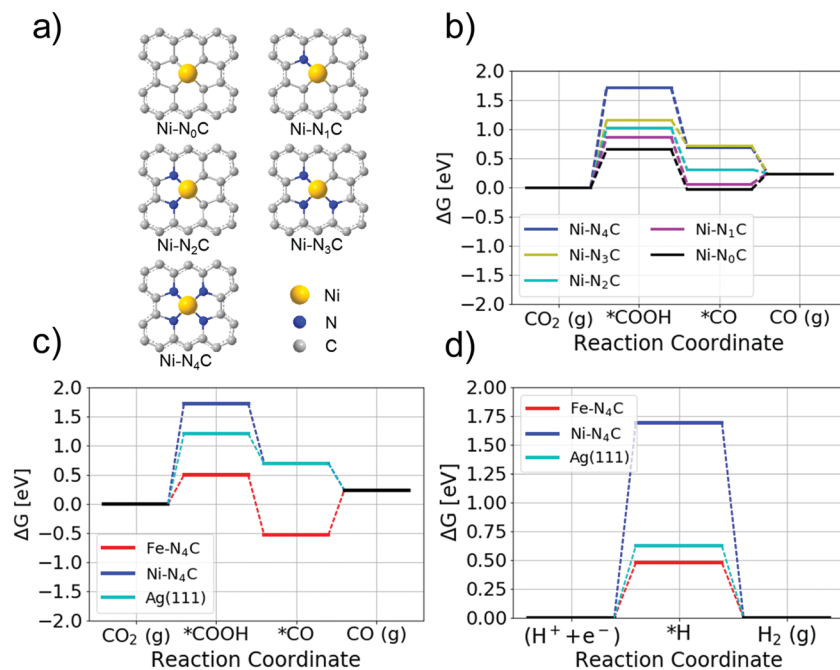


Fig. 3 Free energy diagram of CO₂ reduction to CO on Ni–N–C and Fe–N–C catalysts. (a) Chemical structure of the M–Nx moieties considered, (b) influence of the Ni-coordination on the binding strength for the *COOH and *CO intermediates, (c) Free energy diagram of CO₂ reduction to CO and (d) hydrogen evolution reaction (d) on Fe–N₄–C (red), Ni–N₄–C (blue) and Ag(111) (cyan) catalysts.

we believe the M–N₄ motif and the (111) metal facet models are appropriate for discussing our experimental observations. In our H-cell experiments the Fe–N–C material showed the lowest onset-potential for CO formation, agreeing with the calculated strong *COOH binding, and a decrease of FE_{CO} with ongoing time, which can be indicative of a *CO correlated poisoning caused by strong *CO binding. In contrast, the remarkably high and stable partial current of CO formation on the Ni–N–C catalyst is likely to originate from the ready desorption of CO and sufficiently weak binding of *H, exacerbating HER. Both the DFT calculation and initial H-cell tests indicate the Ni–N–C motif to be a fine catalyst for the CO₂RR to CO.

To assess the technological potential of the Ni–N–C catalysts for industrial CO₂ co-electrolysis, we then turned to single two- and three electrode electrolyzer tests in multi-chambered cell set-ups allowing for pressurized gas flow and circulated electrolyte flows on the anode and cathode (see Fig. 4a).

Mass transport due to the limited solubility of CO₂ is a common problem of CO₂RR tests in CO₂-saturated liquid electrolytes.⁴⁸ This is why we deployed and tested the Ni–N–C catalysts on a Gas Diffusion Electrode (GDE) to be able to approach industrial current densities of several hundred mA cm⁻² geometric electrode area. We utilized spray-coating to apply the catalyst ink onto the commercial carbon GDE substrates with a geometric catalyst loading of 1 mg cm⁻² on an active geometric surface area of 3 cm². The porous nature of the GDE material ensured a sufficient amount of three-phase interface between gaseous CO₂, solid Ni–N–C catalyst, and ionic electrolyte.

During electrolyzer tests, constant current densities between 50 and 700 mA cm⁻² were applied to the cell. Each current

density was held for 2 h before moving to the next current setting. Fig. 4b compares the experimentally measured FE_{CO} values of the four catalysts as a function of the applied cell current densities. Evidently, the Ni–N–C catalyst outperformed the other materials by far in its faradaic efficiency over the entire current density range considered. While the FE_{CO} of the AgO_x catalyst approached that of the Ni–N–C catalyst at low current densities, higher current densities resulted in a sharp drop of CO efficiency on AgO_x due to enhanced HER. The Ni–N–C catalyst reached a maximum FE_{CO} of nearly 90% between 100 and 200 mA cm⁻². The catalyst was able to maintain this impressive performance for 20 hours at 200 mA cm⁻² current density (see Fig. S11, ESI†). A gradual decrease in CO efficiency emerged only at larger current densities of up to 700 mA cm⁻².

The metal-free N–C and the Fe–N–C catalysts were both very inefficient in terms of CO yield under the high current testing conditions. This outcome was expected based on our results from the liquid electrolyte H-cell tests in Fig. 2. There, both catalysts showed reasonable CO efficiencies only up to an electrode potential of roughly -0.6 V vs. RHE. In the case of Fe–N–C, this was the critical electrode potential threshold, where CO poisoning of the Fe–N_x moieties occurred due to strong *CO binding (see Fig. 3). The metal-free NC showed only minor catalytic CO₂RR activity over the entire potential range, due to the absence of active M–N_x functionalities.

Fig. 4c displays the geometric partial CO current densities plotted against the iR-corrected electrode potential of the cathode GDE, made possible by the use of a reference electrode positioned inside the catholyte. The CO partial currents were derived from the experimental FE_{CO} values multiplied by the

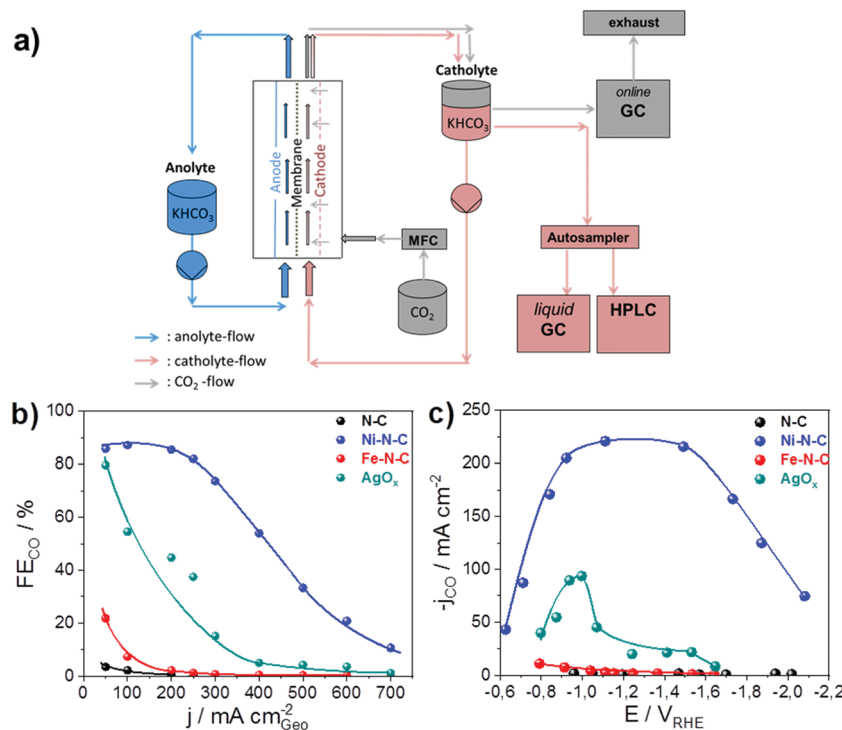


Fig. 4 (a) CO₂ electrolyzer flow cell set up operating at ambient pressures, temperatures and under neutral pH conditions (7.7), incorporating cathodic gas diffusion electrodes; the electrolyzer set-up is equipped with automated robotic liquid sampling ("Autosampler") for automated high pressure liquid chromatographic (HPLC), liquid–gas chromatographic product analysis ("liquid GC"), as well as online chromatographic gas analysis ("online GC"); (b) and (c) Electrolyzer test results under controlled current densities (galvanostatic operation) on N–C (black), Fe–N–C (red), Ni–N–C (blue) and AgO_x (cyan) catalysts. All tests were performed with CO₂ saturated 1 M KHCO₃ and 1 mg cm⁻² catalyst loading. (b) Experimental faradaic CO efficiency as a function of the applied electrolyzer current density. (c) CO partial current density as a function of iR-corrected CO₂ electrode potentials, assessed using a reference electrode. Data points were taken after 120 min of stationary electrolysis at the respective current. Lines are drawn to guide the eye. Complementary electrolyzer polarization curves, CO partial current densities versus the applied current densities and FE_{CO} as a function of applied iR-free potentials are shown in Fig. S9 (ESI†), SEM images before and after electrolysis for the AgO_x and Ni–N–C catalysts in Fig. S10 (ESI†). Stability test of Ni–N–C GDE is presented in Fig. S11 (ESI†).

overall applied current, whereas the iR-corrected potentials were calculated from impedance spectroscopic assessment of the uncompensated ohmic resistances. It is apparent that under the applied current densities the Fe–N–C catalyst operated far outside its optimal electrode potential range, visible in the earlier H-cell measurements. This demonstrates the usefulness of conducting activity screening tests in H-cells in order to properly assess the optimal electrode potential windows of individual CO₂RR catalysts; clearly, on the other hand, the data highlight that H cell screening is not a substitute for catalyst tests under high current densities in GDE configurations of flow electrolyzers. Fig. S9 (ESI†) reports complementary performance data of the electrolyzer tests, including the electrolyzer polarization curves, the dependence of the CO partial current density on the applied current density and the dependence of the FE_{CO} on the applied iR-corrected potential. The polarization curves show a strong dependence on the type of coated catalyst. In accordance to our H-cell experiments, at medium overpotentials (around -0.8 V vs. RHE) the Ni–N–C is the most active material, as a strong CO-binding limits the activity of Fe–N–C. However, upon further increase of current (above 300 mA cm⁻²), we observed a strong loss of CO₂RR activity, FE_{CO} and therefore j_{CO} on the Ni–N–C. Here, we suspect the successive strengthening

of the CO binding on the Ni-motifs with increasing potential⁴⁹ (more negative than -1.2 V vs. RHE) to start limiting further increase of CO₂RR. Fig. S10 (ESI†) compares the surface morphology of the Ni–N–C and the AgO_x catalyst before and after the electrolyzer tests determined by SEM. The Ni–N–C shows a denser coverage on the GDL surface, whereas the AgO_x still seems to expose some of the underlying microporous carbon substrate. This is likely caused by the strong difference in material density and visualizes a lower required mass loading for the N–C class of materials to achieve a full surface coverage. The comparison in terms of CO partial current densities between AgO_x and the Ni–N–C catalyst in Fig. 4c demonstrates the high CO yield of the Ni–N–C catalyst, surpassing 200 mA cm⁻² at -1.0 V vs. RHE, while AgO_x achieves about half that CO yield, however, only in a quite narrow potential range. Another important advantage of the Ni–N–C catalysts relates to the flexibility of their pH operation range. When deployed in fuel cell cathodes, powder M–N–C catalysts were typically operated under either highly acidic or alkaline conditions, depending on whether they served as oxygen reduction catalysts in Proton Exchange Membranes (PEM) or alkaline fuel cells. AgO_x, which reduces to catalytically active metallic Ag at the surface under reaction conditions, is the most commonly deployed catalyst

material for the alkaline CO_2 to CO electrode. Under acidic conditions the catalyst is not stable and dissolves into the electrolyte. AgO_x CO_2RR catalysts are preferable over Au-based, CO_2RR catalysts both due to their improved faradaic efficiencies and cost. Schmid and coworkers utilized commercial silver-based gas diffusion electrodes and reported FE_{CO} values of up to 90% (50 to 300 mA cm^{-2}), consistent with data presented here.²⁷ Kenis and coworkers have used a Ag catalyst ink to fabricate GDEs at high catalyst loadings. In their investigations, they achieved 87% of FE_{CO} at -0.91 V vs. RHE ; however, the total current density of 50 mA cm^{-2} remained relatively low.²⁶ In direct comparison to earlier studies, the performance of the Ni–N–C CO_2RR catalyst presented here equals or exceeds those of previously reported Ag-based catalysts in terms of faradaic CO yield under comparable conditions (see Table S2, ESI†). This demonstrates the great potential of the family of non-metallic M–N–C carbon catalysts, in particular Ni–N–C, for replacing expensive precious group metal catalysts as the benchmark in CO_2 to CO electrolyzers.

Conclusions

We have investigated the electrocatalytic reduction of CO_2 to highly pure CO streams on non-metallic M–N–C carbon catalysts incorporating catalytically active M–N_x single site moieties, where M represented a N-coordinated transition metal ion. The critical role of the M–N_x single site moieties was suggested by the dramatically lower catalytic activity of metal-free nitrogen-doped carbon controls. More specifically, the reactivity and faradaic CO efficiency of Ni–N–C and Fe–N–C single site catalysts were studied both in H-cell based screening tests and in gas diffusion electrode configurations deployed in flow electrolyzers. While Fe–N–C catalysts showed good CO yields at low current densities and overpotentials, the performance of the Ni–N–C catalyst was inferior to those of the Fe–N–C catalysts; at larger current densities and overpotentials Ni–N–C by far outperformed the Fe–N–C catalysts. DFT-based computational analysis revealed the mechanistic origin of the reactivity and selectivity trends between Ni–N–C, Fe–N–C and a model Ag catalyst surface. The chemisorption of CO on the Fe–N_x moiety of the Fe–N–C catalyst is strong and results in CO poisoning and reduced CO efficiencies, while the weaker binding of CO on Ni–N–C and Ag enables larger CO yields at larger current densities and electrode potentials.

The Ni–N–C catalyst outperformed all other tested catalysts with faradaic CO efficiencies of up to 90% and CO partial current densities exceeding 200 mA cm^{-2} in single cell electrolyzer tests. In comparison to previously reported state-of-the-art precious-group-metal Ag electrocatalysts, the Ni–N–C catalysts presented here met or exceeded the single cell performance standard, underlining the great future potential of this group of CO_2RR catalyst materials as an inexpensive substitute for Ag catalysts. Beyond the performance metrics, Ni–N–C catalysts offer flexibility in their pH environment and obvious cost advantages. The family of metal/nitrogen doped carbons, M–N–C, also features a large, to-date unexplored set of choices for the central metal ion M, which holds the promise of other possibly more efficient M–N–C catalyst candidates.

Conflicts of interest

There are no conflicts to declare.

Acknowledgements

P. S. and W. J. acknowledge partial financial support from the German Federal Ministry of Education and Research (Bundesministerium für Bildung und Forschung, BMBF) under grant 03SF0523A “CO2EKAT”. P. S. acknowledges partial financial support from the European Commission under the Horizon2020 – FCH JU 2 program (no. 779366, “CRESCENDO”). A. B. and J. R. thank the Carlsberg Foundation (grant CF15-0165) and the Innovation Fund Denmark (grand solution ProActivE 5124-00003A). W. J. acknowledges the China Scholarship Council (CSC) for financial support. T. M. acknowledges partial financial support from the German Federal Ministry of Education and Research (Bundesministerium für Bildung und Forschung, BMBF) under grant 033RC004E “eEthylene”.

References

- B. Obama, *Science*, 2017, **355**, 126.
- J. M. Spurgeon and B. Kumar, *Energy Environ. Sci.*, 2018, **11**, 1536–1551.
- D. T. Whipple and P. J. A. Kenis, *J. Phys. Lett.*, 2010, **1**, 3451–3458.
- G. Centi, E. A. Quadrelli and S. Perathoner, *Energy Environ. Sci.*, 2013, **6**, 1711.
- A. Bagger, W. Ju, A. S. Varela, P. Strasser and J. Rossmeisl, *ChemPhysChem*, 2017, **18**, 3266–3273.
- Y. Hori, in *Modern Aspects of Electrochemistry*, ed. C. G. Vayenas, R. E. White and M. E. Gamboa-Aldeco, Springer, New York, New York, NY, 2008, pp. 89–189, DOI: 10.1007/978-0-387-49489-0_3.
- A. Murata and Y. Hori, *Bull. Chem. Soc. Jpn.*, 1991, **64**, 123–127.
- A. A. Peterson, F. Abild-Pedersen, F. Studt, J. Rossmeisl and J. K. Norskov, *Energy Environ. Sci.*, 2010, **3**, 1311–1315.
- K. P. Kuhl, E. R. Cave, D. N. Abram and T. F. Jaramillo, *Energy Environ. Sci.*, 2012, **5**, 7050–7059.
- W. Tang, A. A. Peterson, A. S. Varela, Z. P. Jovanov, L. Bech, W. J. Durand, S. Dahl, J. K. Norskov and I. Chorkendorff, *Phys. Chem. Chem. Phys.*, 2012, **14**, 76–81.
- R. Reske, H. Mistry, F. Behafarid, B. R. Cuenya and P. Strasser, *J. Am. Chem. Soc.*, 2014, **136**, 6978–6986.
- H. Mistry, F. Behafarid, R. Reske, A. S. Varela, P. Strasser and B. R. Cuenya, *ACS Catal.*, 2016, **6**, 1075–1080.
- X. Wang, A. S. Varela, A. Bergmann, S. Kühl and P. Strasser, *ChemSusChem*, 2017, **10**, 4642–4649.
- H. Mistry, A. S. Varela, C. S. Bonifacio, I. Zegkinoglou, I. Sinev, Y.-W. Choi, K. Kisslinger, E. A. Stach, J. C. Yang, P. Strasser and B. R. Cuenya, *Nat. Commun.*, 2016, **7**, 12123.
- D. Gao, F. Scholten and B. R. Cuenya, *ACS Catal.*, 2017, **7**, 5112–5120.
- C. W. Li and M. W. Kanan, *J. Am. Chem. Soc.*, 2012, **134**, 7231–7234.

- Published on 13 December 2018. Downloaded by Korea Advanced Institute of Science & Technology / KAIST on 10/24/2023 8:02:02 AM.
- 17 M. García, M. J. Aguirre, G. Canzi, C. P. Kubiak, M. Ohlbaum and M. Isaacs, *Electrochim. Acta*, 2014, **115**, 146–154.
 - 18 C.-T. Dinh, T. Burdyny, M. G. Kibria, A. Seifitokaldani, C. M. Gabardo, F. P. García de Arquer, A. Kiani, J. P. Edwards, P. De Luna, O. S. Bushuyev, C. Zou, R. Quintero-Bermudez, Y. Pang, D. Sinton and E. H. Sargent, *Science*, 2018, **360**, 783.
 - 19 Y. Hori, R. Takahashi, Y. Yoshinami and A. Murata, *J. Phys. Chem. B*, 1997, **101**, 7075–7081.
 - 20 H. Mistry, R. Reske, Z. Zeng, Z.-J. Zhao, J. Greeley, P. Strasser and B. R. Cuenya, *J. Am. Chem. Soc.*, 2014, **136**, 16473–16476.
 - 21 W. Zhu, R. Michalsky, Ö. Metin, H. Lv, S. Guo, C. J. Wright, X. Sun, A. A. Peterson and S. Sun, *J. Am. Chem. Soc.*, 2013, **135**, 16833–16836.
 - 22 W. Zhu, Y.-J. Zhang, H. Zhang, H. Lv, Q. Li, R. Michalsky, A. A. Peterson and S. Sun, *J. Am. Chem. Soc.*, 2014, **136**, 16132–16135.
 - 23 Q. Lu, J. Rosen, Y. Zhou, G. S. Hutchings, Y. C. Kimmel, J. G. Chen and F. Jiao, *Nat. Commun.*, 2014, **5**, 3242.
 - 24 C. Kim, H. S. Jeon, T. Eom, M. S. Jee, H. Kim, C. M. Friend, B. K. Min and Y. J. Hwang, *J. Am. Chem. Soc.*, 2015, **137**, 13844–13850.
 - 25 C. Kim, T. Eom, M. S. Jee, H. Jung, H. Kim, B. K. Min and Y. J. Hwang, *ACS Catal.*, 2017, **7**, 779–785.
 - 26 S. Verma, X. Lu, S. Ma, R. I. Masel and P. J. Kenis, *Phys. Chem. Chem. Phys.*, 2016, **18**, 7075–7084.
 - 27 T. Haas, R. Krause, R. Weber, M. Demler and G. Schmid, *Nat. Catal.*, 2018, **1**, 32–39.
 - 28 V. Tripkovic, M. Vanin, M. Karamad, M. E. Björketun, K. W. Jacobsen, K. S. Thygesen and J. Rossmeisl, *J. Phys. Chem. C*, 2013, **117**, 9187–9195.
 - 29 A. Bagger, W. Ju, A. S. Varela, P. Strasser and J. Rossmeisl, *Catal. Today*, 2017, **288**, 74–78.
 - 30 K. Artyushkova, P. Atanassov, M. Dutta, S. Wessel and V. Colbow, *J. Power Sources*, 2015, **284**, 631–641.
 - 31 K. Artyushkova, B. Kiefer, B. Halevi, A. Knop-Gericke, R. Schlogl and P. Atanassov, *Chem. Commun.*, 2013, **49**, 2539–2541.
 - 32 K. Artyushkova, S. Pylypenko, M. Dowlapalli and P. Atanassov, *J. Power Sources*, 2012, **214**, 303–313.
 - 33 E. F. Holby, G. Wu, P. Zelenay and C. D. Taylor, *J. Phys. Chem. C*, 2014, **118**, 14388–14393.
 - 34 S. Kattel, P. Atanassov and B. Kiefer, *Phys. Chem. Chem. Phys.*, 2013, **15**, 148–153.
 - 35 T. N. Huan, N. Ranjbar, G. Rousse, M. Sougrati, A. Zitolo, V. Mougel, F. Jaouen and M. Fontecave, *ACS Catal.*, 2017, **7**, 1520–1525.
 - 36 W. Ju, A. Bagger, G.-P. Hao, A. S. Varela, I. Sinev, V. Bon, B. Roldan Cuenya, S. Kaskel, J. Rossmeisl and P. Strasser, *Nat. Commun.*, 2017, **8**, 944.
 - 37 N. Leonard, W. Ju, I. Sinev, J. Steinberg, F. Luo, A. S. Varela, B. Roldan Cuenya and P. Strasser, *Chem. Sci.*, 2018, **9**, 5064–5073.
 - 38 P. Su, K. Iwase, S. Nakanishi, K. Hashimoto and K. Kamiya, *Small*, 2016, **12**, 6083–6089.
 - 39 X. Li, W. Bi, M. Chen, Y. Sun, H. Ju, W. Yan, J. Zhu, X. Wu, W. Chu, C. Wu and Y. Xie, *J. Am. Chem. Soc.*, 2017, **139**, 14889–14892.
 - 40 C. Yan, H. Li, Y. Ye, H. Wu, F. Cai, R. Si, J. Xiao, S. Miao, S. Xie, F. Yang, Y. Li, G. Wang and X. Bao, *Energy Environ. Sci.*, 2018, **11**, 1204–1210.
 - 41 K. Jiang, S. Siahrostami, T. Zheng, Y. Hu, S. Hwang, E. Stavitski, Y. Peng, J. Dynes, M. Gangisetty, D. Su, K. Attenkofer and H. Wang, *Energy Environ. Sci.*, 2018, **11**, 893–903.
 - 42 K. Jiang, S. Siahrostami, A. J. Akey, Y. Li, Z. Lu, J. Lattimer, Y. Hu, C. Stokes, M. Gangishetty, G. Chen, Y. Zhou, W. Hill, W.-B. Cai, D. Bell, K. Chan, J. K. Nørskov, Y. Cui and H. Wang, *Chem*, 2017, **3**, 950–960.
 - 43 G. Wu, K. L. More, C. M. Johnston and P. Zelenay, *Science*, 2011, **332**, 443–447.
 - 44 N. Ranjbar Sahraie, J. P. Paraknowitsch, C. Göbel, A. Thomas and P. Strasser, *J. Am. Chem. Soc.*, 2014, **136**, 14486–14497.
 - 45 N. D. Leonard, S. Wagner, F. Luo, J. Steinberg, W. Ju, N. Weidler, H. Wang, U. I. Kramm and P. Strasser, *ACS Catal.*, 2018, **8**, 1640–1647.
 - 46 S. Kabir, K. Artyushkova, B. Kiefer and P. Atanassov, *Phys. Chem. Chem. Phys.*, 2015, **17**, 17785–17789.
 - 47 S. Varela Ana, N. Ranjbar Sahraie, J. Steinberg, W. Ju, H. S. Oh and P. Strasser, *Angew. Chem., Int. Ed.*, 2015, **54**, 10758–10762.
 - 48 N. Gupta, M. Gattrell and B. MacDougall, *J. Appl. Electrochem.*, 2006, **36**, 161–172.
 - 49 P. Su, K. Iwase, T. Harada, K. Kamiya and S. Nakanishi, *Chem. Sci.*, 2018, **9**, 3941–3947.
 - 50 A. S. Varela, W. Ju and P. Strasser, *Adv. Energy Mater.*, 2018, **8**, 1703614.